Atomic-force-microscope study of contact area and friction on $NbSe_2$

M. A. Lantz, S. J. O'Shea, and M. E. Welland
Engineering Department, Cambridge University, Cambridge CB2 1PZ, United Kingdom

K. L. Johnson
1 New Square, Cambridge CB1 1EY, United Kingdom

(Received 25 November 1996)

We have used an ultrahigh vacuum atomic-force microscope to study the variation in contact radius and friction with applied force between a silicon tip and a $NbSe_2$ sample. The data are compared to the Maugis-Dugdale theory, which is the appropriate continuum mechanics model for the properties and size of the tip-sample contact. The lateral stiffness of the tip-sample contact is related to the radius of the tip-sample contact through the shear moduli of the materials and we have used this relationship to measure directly the variation in contact radius with applied load. The contact radius measured in this way is found to be in agreement with the Maugis-Dugdale theory using the bulk values of the shear moduli. We also measured the variation in friction force with applied load using the same silicon tip. The variation in friction force with applied normal force is found to follow the variation of the contact area as predicted by the Maugis-Dugdale theory [D. Maugis, J. Colloid Interface Sci. **150**, 243 (1992)], which supports the hypothesis that for a single asperity contact, the frictional shear stress τ is constant. The value of the shear stress is found to be $\tau \approx 6 \times 10^8$ N/m^2, which is comparable to the estimated theoretical shear strength of $NbSe_2$. [S0163-1829(97)05916-X]

I. INTRODUCTION

The atomic- and friction-force microscopes (AFM and FFM) are important new tools in the field of tribology. Since the development of the FFM by Mate *et al.*[1] and their initial observations of atomic scale slip-stick motion, applications of the AFM and FFM to tribology have grown rapidly. Interest has been motivated by the high spatial and force resolution attainable with these techniques as well as by the single asperity nature of the contact formed between the AFM/FFM tip and sample. It is hoped that new insight into the fundamental mechanisms of tribological phenomena can be gained using these techniques.

One question of fundamental importance in tribology is the relation between friction and contact area. For the case of dry sliding, Bowden and Tabor first proposed that in the absence of ploughing, friction is directly proportional to the real area of contact between surfaces,[2] i.e.,

$$F_{\text{friction}} = \tau A, \tag{1}$$

where A is the real area of contact and τ is the shear strength of the contact. Most surfaces are rough on the microscale and contact only occurs between the surface asperities; the real area of contact is therefore much smaller than the apparent contact area. When a normal force is applied between the two surfaces, the surfaces deform elastically and/or plastically and the contact area increases. For randomly rough surfaces, the real area of contact increases in direct proportion to the normal force, in which case Amonton's law that friction is proportional to the applied force is recovered from Eq. (1).

The single asperity nature of the contact formed between an AFM tip and sample would seemingly make it ideal for investigating the relation between friction and real contact area. Unfortunately, the direct measurement of the contact area between an AFM tip and sample is not a trivial problem and AFM investigations of friction have relied on contact mechanics theories to relate friction to area. This approach requires knowledge of the tip geometry if quantitative measurements of the contact area and shear strength are to be made. With a few noted exceptions (for example, see Refs. 3 and 4), this has restricted most AFM friction studies to qualitative comparisons between theory and experiment. In addition, many FFM investigations of dry sliding have been carried out in air where the tip and sample are inevitably covered in a few monolayers of water and other absorbed contaminants. This lack of control over the tip-sample interface makes the interpretation of data and comparison between experiments difficult.

In order to overcome these problems, we have constructed an ultrahigh vacuum (UHV) AFM to study friction and point contacts. In an earlier paper we demonstrated how the lateral stiffness of the tip-sample contact can be related to the tip-sample contact area, provided the geometry of the AFM tip is well characterized.[5] For tip characterization, we use a scanning transmission electron microscope (STEM) to image the apex of the tip and measure the tip radius, before and after the experiments. In this paper, we demonstrate the use of the contact stiffness technique to measure the contact radius as a function of applied normal force between a Si AFM tip and a $NbSe_2$ sample in UHV. Using the same tip and sample we also measure friction force as a function of applied normal force. Quantitative comparisons are then made between these two sets of data and a continuum model for a spherical point contact (the Maugis-Dugdale theory[6,7]).

II. THEORETICAL BACKGROUND

A variety of theories can be used to model the elastic contact between an AFM tip and sample under normal applied forces. When the adhesive force between the tip and sample is negligible compared to the applied force, Hertz theory can be used.[8,9] In the regime where adhesive forces are comparable to the applied normal force, the analysis is more complex. The ratio of elastic deformation in the contact to the distance over which surface forces act can be expressed by the nondimensional parameter ϕ, given by[10]

$$\phi=\left(\frac{Rw^2}{E^{*2}z_0^3}\right)^{1/3}. \tag{2}$$

Here R is the radius of the tip, w is the work of adhesion (equal to twice the surface energy), z_0 is the equilibrium spacing for the Lennard-Jones potential of the surfaces, and E^* is the combined elastic modulus of the tip and sample, given by

$$E^*=\left(\frac{1-\nu_1^2}{E_1}+\frac{1-\nu_2^2}{E_2}\right)^{-1}, \tag{3}$$

where $\nu_{1,2}$ are the Poisson's ratios and $E_{1,2}$ are Young's moduli for the tip and sample, respectively. When ϕ is large ($\phi>5$) the Johnson-Kendall-Roberts (JKR) theory[11] provides a good approximation of the elastic deformation in the contact and when ϕ is small ($\phi<0.1$) elastic deformation is negligible and the analysis by Bradley[12] or the Derjaguin-Muller-Toporov (DMT) model[13] is more appropriate.[7,8] In the intermediate regime, the Maugis-Dugdale theory[6,7] provides an approximate closed-form analysis and this is the model we adopt in this work, because for typical AFM operation with sharp tips, $\phi\sim1$. We shall now outline the Maugis-Dugdale theory in sufficient detail to highlight the computational procedure followed. A more complete description is given by Johnson.[7]

The Maugis-Dugdale theory describes the adhesion and separation in a purely elastic spherical contact under a normal load. Intimate contact (zero separation) between the two surfaces occurs within a circular area of radius a, as illustrated in Fig. 1(a). The attractive interaction between the surfaces extends over a larger circular region, with radius c. In the region between c and a the surfaces separate slightly by a distance increasing from zero at $r=a$ to h_0 at $r=c$. The adhesive force between the two surfaces is assumed to have a constant value σ_0 until a separation h_0 is reached, at which point the adhesive force falls to zero as shown in Fig. 1(b). This is the Dugdale approximation. The value of h_0 is chosen such that the maximum attractive force and the work of adhesion match those of a Lennard-Jones potential, i.e., $\sigma_0 h_0=w_{\mathrm{LJ}}$ hence $h_0=0.971z_0$.

The distribution of pressure within the contact is composed of two terms: the Hertz pressure $p_1(r)$ associated with a contact of radius a,

$$p_1(r)=\frac{3P_1}{2\pi a^2}\left[1-(r/a)^2\right]^{1/2}, \tag{4}$$

where

$$P_1=4E^*a^3/3R, \tag{5}$$

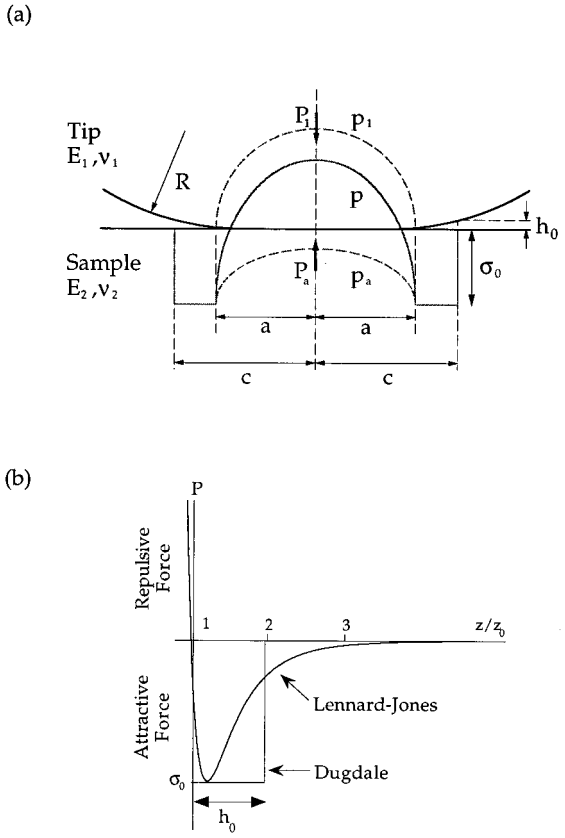

FIG. 1. (a) Maugis-Dugdale model of the tip-sample contact. Intimate contact occurs within a circular region with radius a. A constant attractive force σ_0 continues to act over a larger circular region, with radius c. The pressure distributions (p) across the contact are also shown. (b) Lennard-Jones and Dugdale force laws. h_0 is chosen such that the maximum attractive force and the area under the attractive part of the force curves match, i.e., $\sigma_0 h_0=w_{\mathrm{LJ}}$.

and an adhesive (Dugdale) component

$$p_a(r)=\begin{cases}-(\sigma_0/\pi)\cos^{-1}\left(\dfrac{2a^2-c^2-r^2}{c^2-r^2}\right), & r\leqslant a\\ -\sigma_0, & a\leqslant r\leqslant c\end{cases} \tag{6}$$

which corresponds to an adhesive force P_a, given by

$$P_a=-2\sigma_0\left[c^2\cos^{-1}(a/c)+a\sqrt{c^2-a^2}\right]. \tag{7}$$

The net force P acting on the contact is then $P=P_1+P_a$. The values of a and c can be found by simultaneously solving the two equations

$$\frac{\lambda\overline{a^2}}{2}\left[(m^2-2)\cos^{-1}\left(\frac{1}{m}\right)+\sqrt{m^2-1}\right]+\frac{4\lambda^2\overline{a}}{3}\left[\sqrt{m^2-2}\,\cos^{-1}\left(\frac{1}{m}\right)-m+1\right]=1 \tag{8}$$

and

$$\overline{P}=\overline{P_1}+\overline{P_a}=\overline{a^3}-\lambda\overline{a^2}\left[\sqrt{m^2-1}+m^2\cos^{-1}(1/m)\right], \tag{9}$$

where $m=c/a$ and $\overline{a}$, $\overline{c}$, $\overline{P}$, and λ are nondimensional parameters defined as

$$\overline{a} \equiv a\left(\frac{4E^*}{3\pi w R^2}\right)^{1/3}, \quad \overline{c} \equiv c\left(\frac{4E^*}{3\pi w R^2}\right)^{1/3},$$

$$\overline{P} \equiv \frac{P}{\pi w R}, \quad \lambda = 2\sigma_0\left(\frac{9R}{16\pi w E^{*2}}\right).$$

It can be shown that $\lambda = 1.16\phi$, so that λ is also a measure of the ratio of elastic deformation to the range of surface forces. We assume that the effective radius b over which friction forces act, lies somewhere between a and c, thus

$$b = a + n(c-a), \tag{10}$$

where $0 < n < 1$. For example, when comparing friction data to the theory we can write Eq. (1) as $F_{\text{friction}} = \tau A = \tau\pi b^2$. In this work we assume that $n = 0.4$, as this corresponds approximately to the maximum attractive force in the Lennard-Jones interaction potential. In addition, good agreement has been obtained between previously reported UHV AFM friction data and Eq. (1) using the Maugis-Dugdale theory with $n = 0.4$.[7]

Equations (8) and (9) have real-valued solutions up to a critical value P_c, where $P_c < 0$, indicating that a finite contact area exists at negative applied forces. This separation or pull-off force P_c is given by the minimum value of P for which real values of a and c satisfy Eqs. (8) and (9) and is therefore a function of R, E^*, w, and λ. If R and E^* are known, then w and λ can be calculated using the experimentally measured pull-off force P_c and an iterative technique [Eqs. (2), (8), and (9) and the relation $\lambda = 1.16\phi$]. In our experiments, the radius of the tip R is measured using a STEM and E^* is calculated using bulk material properties. Once λ and w have been found, the variation in the contact radii a and c can be solved for as a function of the total normal force P. For comparison, we have measured the tip-sample contact radius as a function of P directly through the stiffness of the tip-sample contact. This method will now be discussed in detail.

III. TIP-SAMPLE CONTACT STIFFNESS

If a lateral force smaller than the force of limiting friction is applied to the tip-sample contact by laterally displacing the sample a small distance, then the contact between the tip and sample will deform elastically and distant points in the tip and sample will be laterally displaced from each other. If we model the tip and sample as a sphere on a flat [see Fig. 2(a)] and assume that (i) there is no coupling between normal and lateral forces and (ii) the lateral force Q_x acting on the contact is small compared with the limiting friction force, then the lateral displacement $\delta_x = \delta_{x1} + \delta_{x2}$ between distant points T_1 in the tip and T_2 in the sample is[8]

$$\delta_x = \frac{Q_x}{8b}\left(\frac{2-\nu_1}{G_1} + \frac{2-\nu_2}{G_2}\right) = \frac{Q_x}{8bG^*}. \tag{11}$$

Here b is the radius of the contact, $G_{1,2}$ are the shear moduli of the tip and sample, respectively, and G^* is the effective shear modulus of the tip and sample given by

$$G^* = \left(\frac{2-\nu_1}{G_1} + \frac{2-\nu_2}{G_2}\right)^{-1}. \tag{12}$$

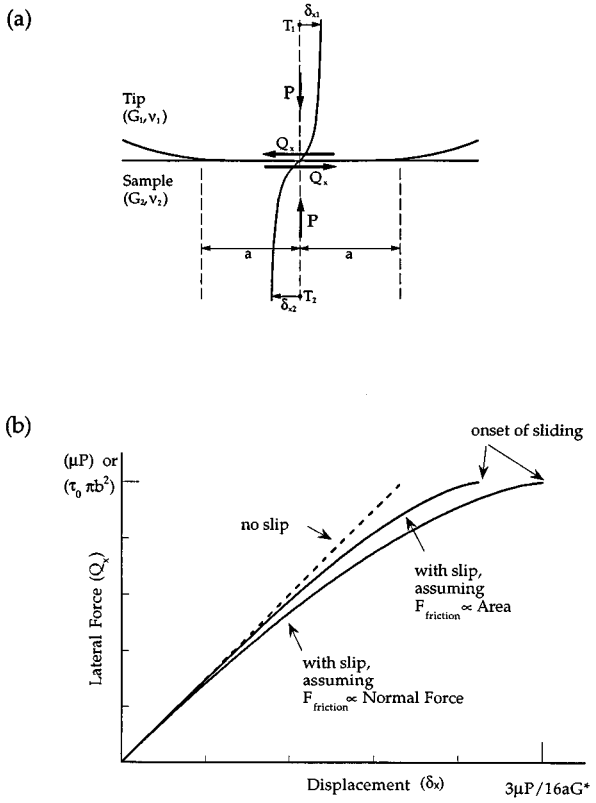

FIG. 2. (a) Sphere on flat model of tip-sample contact. Here distant points in the tip and sample are displaced from each other by a distance $\delta_x = \delta_{x1} + \delta_{x2}$ by the lateral force Q_x. (b) Plot of lateral force Q_x versus displacement of distance points in the tip and sample δ_x: ----, no slip; —, with slip. Gross sliding begins when the lateral force equals the force of limiting friction.

The assumption that there is no interaction between normal and lateral forces is strictly valid only if the elastic constants of the tip and sample are the same. However, the correction required if the elastic constants are different is generally small and will be neglected here.[8]

The second assumption that the contact does not slip is also somewhat unrealistic, as the tangential traction necessary to prevent slip is theoretically infinite at the contact periphery. A limited amount of slip (microslip), therefore, must occur at the edge of the contact, even for very small lateral forces. As the lateral force is increased, the region of microslip extends towards the center of the contact until the force of limiting friction is exceeded, at which point the entire contact slips and the tip begins to slide. To account for this effect, we must assume a tangential traction (friction) distribution for the contact.

In macroscopic sliding, we would expect the friction traction to be proportional to the applied force (Amonton's law). For this case, if we relax the assumption that no slip occurs and assume that the friction is proportional to a Hertzian contact pressure, then the relative displacement δ_x of distant points in the tip and sample is given by[8]

$$\delta_x = \frac{3\mu P}{16aG^*}\left[1 - \left(1 - \frac{Q_x}{\mu P}\right)^{2/3}\right], \tag{13}$$

where μP is the force of limiting friction.

Alternatively, for a single asperity contact, as for AFM, we expect that friction is directly proportional to the contact area, i.e., Eq. (1) ($F_{\text{friction}}=\tau A=\tau\pi b^2$). When a lateral force Q_x is applied to the contact, microslip occurs at the contact periphery. If we define the inner radius to which the microslip has penetrated as e and assume that Eq. (1) also holds in the region of the microslip, then the relative displacement δ_x of distant points in the tip and sample due to a lateral force Q_x is given by[9]

$$Q_x=2\tau b^2[\cos^{-1}\gamma+\gamma\sqrt{1-\gamma^2}] \tag{14}$$

and

$$\delta_x=\frac{\tau b}{2G^*}\sqrt{1-\gamma^2}, \tag{15}$$

where $\gamma=e/b$ ranges from $\gamma=1$ when $Q_x=0$ to $\gamma=0$ when $Q_x=\tau\pi b^2$ (the limiting force of friction).

Equations (11) and (13)–(15) have been plotted in Fig. 2(b). It is apparent from the figure that for lateral forces well below the force of limiting friction, Eqs. (13)–(15) are well approximated by Eq. (11). Thus, regardless of whether Eq. (1) or Amonton's law is obeyed, we can use Eq. (11) to approximate the contact stiffness for small lateral forces, i.e.,

$$k_{\text{contact}}=Q_x/\delta_x=8aG^*. \tag{16}$$

Therefore, by measuring k_{contact} we can solve for the contact radius using the bulk material properties of the tip and sample. In addition, the variation in contact radius with applied force can be directly measured and compared to the contact radius predicted by the Maugis-Dugdale theory. This approach has a general similarity to the method whereby forces and displacements in the direction normal to the surface are measured,[14] in which case $k_{\text{contact}}\approx 2aE^*$.

In the experimental procedure used to find k_{contact}, a known lateral displacement is applied to the sample and the resulting force acting on the contact is measured. The compliance of the contact is then calculated, taking into account the additional compliances of the tip and the cantilever. We model the behavior of the cantilever, tip, and tip-sample contact under the influence of a small lateral displacement as three coupled springs in series, as illustrated in Fig. 3. A lateral displacement of the sample Δx will be distributed between the three compliant elements. The contact stiffness is given by

$$k_{\text{contact}}=\left[\frac{\Delta x}{F_{\text{lateral}}}-\frac{1}{k_{\text{lateral}}}-\frac{1}{k_{\text{tip}}}\right]^{-1}, \tag{17}$$

where $1/k_{\text{tip}}$ and $1/k_{\text{lateral}}$ are the lateral compliances of the tip and cantilever, respectively. Thus, if k_{lateral} and k_{tip} are known, the contact stiffness k_{contact} can found by measuring the lateral force acting on the tip due to a small displacement of the sample Δx. It is important to note that when $\Delta x/F_{\text{lateral}}$ becomes comparable to $1/k_{\text{lateral}}+1/k_{\text{tip}}$, i.e., when the contact stiffness becomes large, the error in the measured contact stiffness increases rapidly. Thus the range of contact stiffness and contact radii that can be measured using this technique is limited by the combined lateral stiffness of the tip and cantilever.

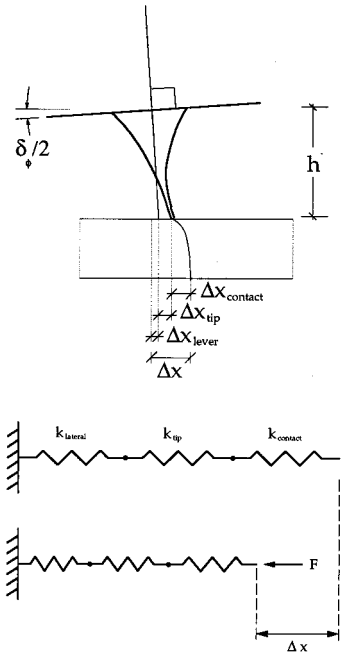

FIG. 3. Model of compliant tip and tip-sample contact showing the response of the various springs (k) to a lateral force (F). The lateral displacements (Δx) shown are greatly enlarged. Typically $h\sim 3-15\ \mu$m and $\Delta x<5$ Å. Experimentally, the angular change $\delta_\phi/2$ is measured.

For the above technique to be accurate, the lateral stiffness of the tip and cantilever must be known. In our experiments we use a rectangular cantilever microfabricated from single-crystal silicon.[15] It is simpler and more accurate to analyze the mechanical behavior of such cantilevers compared to the commonly used triangular-shaped Si_3N_4 AFM cantilevers. The lateral and normal spring constants of the cantilever were calculated to be $k_{\text{normal}}=1.1$ N/m and $k_{\text{lateral}}=110$ N/m using the formulas[16]

$$k_{\text{normal}}=EWt^3/4c \tag{18}$$

and

$$k_{\text{lateral}}=GWt^3/3ch^2. \tag{19}$$

Here E is Young's modulus and G is the shear modulus of Si ($E=169$ GPa and $G=60$ GPa (Ref. 17) for the [110] direction); W and t are the width and thickness of the cantilever, respectively, c is the length of the cantilever from the base to the tip, and h is the length of the tip measured from the neutral axis of the cantilever. The length and width of the cantilever and the height and position of the tip were measured from images of the cantilever and tip taken after the experiments using a Cambridge Instruments scanning electron microscope (SEM). It is difficult to accurately measure the thickness of the cantilever using SEM images due to the scattering of electrons off the faces of the cantilever. We therefore used the technique of Nonnenmacher *et al.*[18] to determine the thickness of the cantilever using the measured resonant frequency of the unloaded cantilever.

The lateral stiffness of the tip k_{tip} used in this experiment was determined using a finite element model. The model was

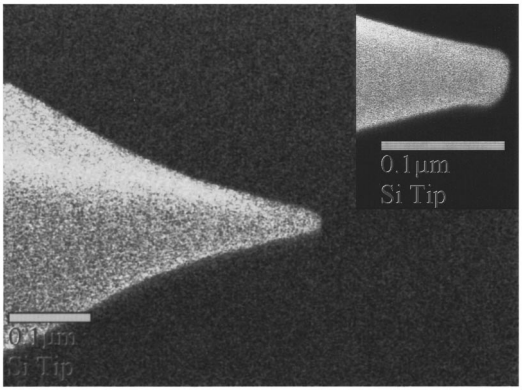

FIG. 4. (a) STEM backscatter image of the original Si tip. $R_{\text{tip}} = 12$ nm and $k_{\text{tip}} = 84$ N/m. (b) STEM backscatter image of the Si tip after intentional blunting. $R_{\text{tip}} = 45$ nm and $k_{\text{tip}} = 108$ N/m.

constructed using the geometry measured from images of the tip apex taken with a JEOL 4000 EX scanning transmission electron microscope. Details are given elsewhere.[5] We only note that k_{tip} is of the same order as k_{lateral} and therefore must be considered in our simple spring model of the experiment. A relatively low value of k_{tip} appears to be common for high-aspect-ratio AFM tips.[5] For example, Fig. 4 shows STEM images of the tip used in the present experiments. Figure 4(a) shows the original tip, as received from the manufacturer, and Fig. 4(b) shows the tip after it had been intentionally blunted. The stiffnesses were determined to be $k_{\text{tip}} = 84$ N/m before blunting and $k_{\text{tip}} = 108$ N/m after blunting. For comparison, the lateral cantilever stiffness calculated using Eq. (19) is $k_{\text{lateral}} = 110$ N/m.

IV. EXPERIMENT

The experiments were performed using a home-built optical-deflection-type UHV AFM. In this system, the tip is fixed and the sample is scanned using a piezoelectric tube scanner. The microscope can also be operated as a scanning tunneling microscope and the tube scanner was calibrated for small displacements using atomic resolution images of silicon taken in the STM mode. Samples can be cleaned *in situ* by heating and argon-ion sputtering. The base pressure in the system is 5×10^{-10} Torr.

Sample preparation consisted of cleaving a $NbSe_2$ sample immediately prior to transfer into vacuum and then heating to 120 °C for 30 min prior to each experiment. The Si tip was imaged as received from the manufacturer in the STEM and then transferred into the vacuum system. Before transfer into the main UHV chamber, the tip was baked out in the load lock chamber at 120 °C for 12 h. No other attempt was made to clean the tip after imaging it in the STEM to avoid modifying the tip's geometry. The tip's surface is therefore expected to be a thin native oxide layer. Before performing the contact stiffness and friction experiments, the $NbSe_2$ was imaged in contact mode at an applied force of a few nanonewtons. Images revealed flat terraces with well-spaced single atomic steps. Contact stiffness and friction measurements were performed near the center of large terraces to avoid any anomalies that might occur due to the topography. No modification of the surface was detectable in images taken before and after the experiments.

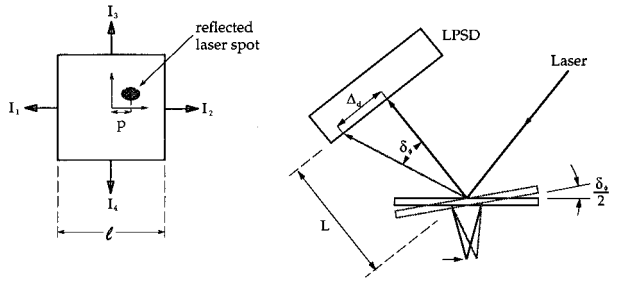

FIG. 5. Schematic of tetralateral LPSD used for the AFM. Four orthogonal currents (I_{1-4}) allow both lateral and normal angular displacements ($\delta_\phi/2$) of the cantilever to be measured.

In order to measure both lateral and normal forces simultaneously, we have adopted the method of Meyer and Amer[19] in which a quadrant photodiode is used to separate the measured deflection of the laser beam into two orthogonal components. However, rather than the four-segment photodiode conventionally used for the FFM, we used a linear position-sensitive detector (LPSD).[20] Although the output of LPSD's is typically two to three times noisier then that of segmented diodes, they have the advantage of measuring the absolute position of the centroid of the reflected light spot and are indifferent to the spot's shape or intensity distribution. This permits the angular displacements of the cantilever to be measured directly (as detailed below) without the calibration required for segmented detectors.[21]

Figure 5 illustrates the measurement of an angular displacement of a cantilever due to a lateral displacement of the sample using a tetralateral LPSD. If I_1 and I_2 are the lateral position current outputs of the LPSD, then the lateral position p of the centroid of the reflected laser spot is given by

$$p = \left(\frac{I_1 - I_2}{I_1 + I_2} \right) \frac{l}{2}, \tag{20}$$

where l is the width of the active area of the LPSD. The change in the spot position Δd is simply the difference between the position before and after the lateral displacement of the tip. The angular displacement of the cantilever $\delta_\phi/2$ is then given by

$$\frac{\delta_\phi}{2} = \frac{1}{2} \tan^{-1}\left(\frac{\Delta d}{L} \right), \tag{21}$$

where L is the distance between the cantilever and the LPSD. The lateral force acting on the tip is given by

$$F_{\text{lateral}} = k_{\text{lateral}}[h \tan(\delta_\phi/2)], \tag{22}$$

where h is the length of the tip.

The accuracy of the measured angular displacement is limited by the noise in the photodetector current and how accurately the path length L and the width of the detector l are known. However, in calculating the lateral force, we find that the dominant source of error arises from the uncertainty in how close the laser spot is positioned to the base of the tip.[22] This is because the angular displacement of the cantilever due to a lateral force acting on the tip varies linearly from 0° at the base of the cantilever to its maximum value at

the free end of the lever.[23] Combined with the uncertainty in the lateral spring constant, we estimate the uncertainty in the measured lateral force to be $\pm 20\%$. The measurement of normal forces is analogous to the lateral force measurement procedure and the uncertainty in the measured normal force is comparable to that of the lateral force. In most of our experiments we are concerned with how the lateral force varies with the applied normal force and in these cases the relative error between the two measured forces is significantly smaller than the absolute error.

V. RESULTS

A. General procedure

In these experiments, the $NbSe_2$ sample was displaced laterally (perpendicular to the long axis of the cantilever) using a triangular wave form applied to the piezoscan tube. The resulting angular displacement of the cantilever was measured using the LPSD. The magnitude of the lateral displacement signal was measured using a lock-in amplifier and monitored simultaneously on an oscilloscope. The dependence of the angular displacement [and hence, using Eq. (22), the lateral force] on the applied force can be found by pulling the tip off the surface and simultaneously logging the lock-in amplifier signal and the normal deflection of the cantilever. Such data are referred to as a force-distance curve. We generally retract the tip from the surface, i.e., unload, as this allows the adhesive force minima to be sampled and the pull-off force to be measured. Typical unloading speeds are ~ 2 nm/s, which is sufficiently slow for good lock-in averaging and fast enough such that thermal drift is not a problem.

Two types of force-distance experiments are done, static and sliding, differing in that either a small or large displacement is applied to the sample. For a sufficiently small displacement, the tip does not slip and changes in the lock-in signal as the applied force is decreased correspond to changes in the stiffness of the contact k_{contact}. We can then relate the variation in contact stiffness with applied normal force to the contact radius using Eq. (16). At larger lateral displacements, the tip slides and the lock-in signal corresponds to changes in the static friction force. In both cases, it is important to observe the shape of the angular displacement signal on the oscilloscope during the measurement to ensure that the tip is (or is not) sliding.

B. Static contact stiffness measurement

The stiffness of the contact was measured by applying an 80-Hz triangular voltage wave form to the scan tube, giving a lateral displacement of the sample of $\Delta x = 3.7$ Å peak to peak. An example is shown in Fig. 6, which shows the driving wave form and the lateral displacement of the cantilever $[\Delta x_{\text{lever}} = h \tan(\delta_d/2)]$ at an applied force of 4.5 nN. We note that the cantilever displacement is slightly phase shifted relative to the driving wave form, due to the mechanical response time of the scan tube and that the cantilever displacement linearly follows the driving wave form, indicating that the sample is not slipping relative to the tip [refer to Fig. 2(b)]. The cantilever movement is considerably less than the movement being imposed on the tip by the sample. This is because the tip and tip-sample contact are not infinitely stiff but consist of the additional compliances $1/k_{\text{tip}}$ and $1/k_{\text{contact}}$.

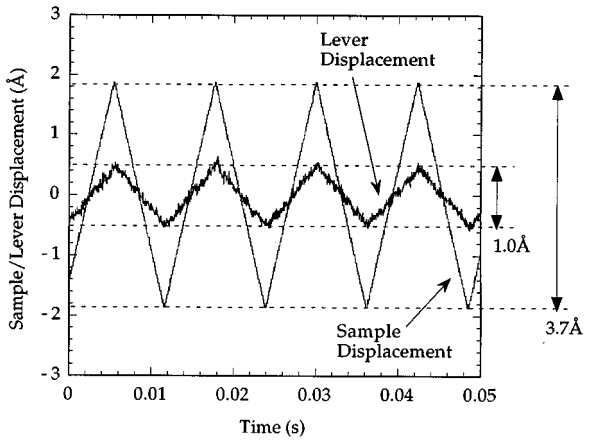

FIG. 6. Lateral response of cantilever due to the 3.7-Å peak-to-peak displacement of the $NbSe_2$ sample. The applied normal force is 4.5 nN.

The amplitude of the lever displacement signal varies as the applied force changes because k_{contact} depends on the applied normal force. This is most clearly seen in a force-distance curve. Figure 7 shows the result of a typical experiment. Taking the values given previously of $k_{\text{lateral}} = 110$ N/m, $k_{\text{tip}} = 84$ N/m, and $\Delta x = 3.7$ Å peak to peak, we can calculate the contact stiffness using Eq. (17). In Fig. 8, the contact stiffness has been plotted versus the applied normal force for the data of Fig. 7. We observe that the contact stiffness is comparable to that of the tip and cantilever and decreases rapidly near the separation force P_c, as expected theoretically. It is important to note that small uncertainties in the variables of Eq. (17) can result in large errors in the calculated contact stiffness, especially at larger normal forces where the magnitude of the contact stiffness is large compared to the combined lateral stiffness of the tip and cantilever. This is observed in the raw data of Fig. 7, where changes in the lateral force are more obvious near tip-sample separa-

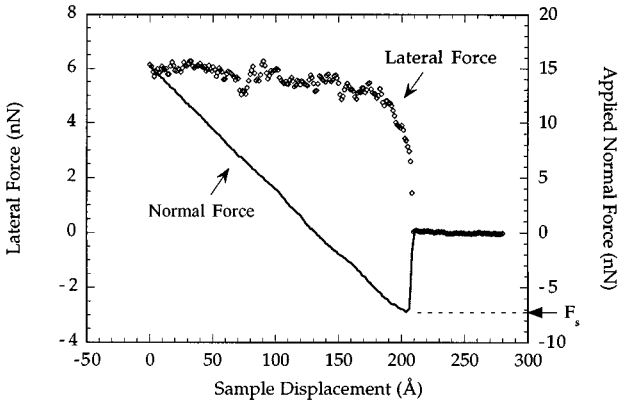

FIG. 7. Force-distance experiment lateral force as a function of applied normal force. The sample displacement is the movement of the z piezo. The displacement zero is arbitrary. The tip and sample separate as the displacement becomes more positive and separation occurs at 210 Å.

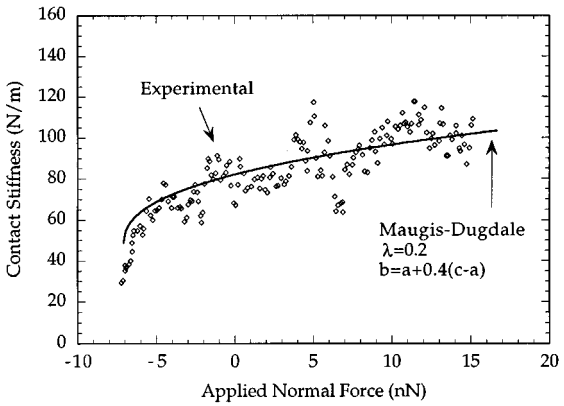

FIG. 8. Contact stiffness versus applied normal force calculated from the data of Fig. 7 using Eq. (17). The solid line is the Maugis-Dugdale fit to the data.

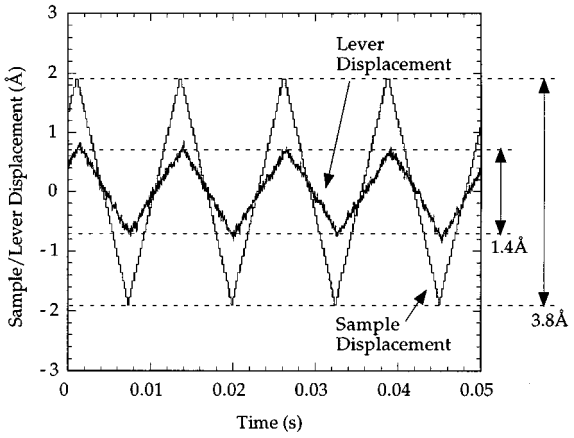

FIG. 9. Lateral response of the cantilever after blunting the tip. The sample displacement is 3.8 Å peak to peak and the applied normal force is −3.3 nN.

tion. As an example, at an applied normal force of 4.5 nN (Fig. 6), an uncertainty of 5% in Δx results in an uncertainty of 15% in k_{contact}. The total uncertainty in the contact stiffness measured from the data of Fig. 6 is approximately ±50%. This uncertainty increases with applied normal force.

Using the separation force measured from Fig. 8 ($P_c = -7.0$ nN) and the tip radius as measured from STEM images ($R_{\text{tip}} = 12$ nm), we can use the Maugis-Dugdale theory to calculate the work of adhesion w and the elasticity parameter λ. Taking the interaction distance to be $z_0 = 0.2$ nm and the combined elastic modulus for Si and $NbSe_2$ to be $E^* = 40.3$ GPa,[17,24] we calculate values of $\lambda = 0.2$ and $w = 0.099$ J/m^2. These values of λ, w, z, E^*, and R_{tip} can then be used to calculate the contact radii a and c predicted by the Maugis-Dugdale theory. In order to compare the experimental contact stiffness data with the Maugis-Dugdale theory we recall that k_{contact} is proportional to the contact radius. Hence we can scale the Maugis-Dugdale value of the contact radius, given by $b = a + 0.4(c - a)$, to the experimental values of k_{contact} by forcing the two values to match at a point on the experimental contact stiffness curve. (We have used k_{contact} at $P = 0$.) The Maugis-Dugdale fit has been plotted in Fig. 8 for the experimental range of applied forces and is in good agreement with the experimental data. This fit only shows that the variation with applied force is well represented by the theory. To test the physical consistency of our modeling we can use the contact radius predicted by the Maugis-Dugdale theory to calculate the effective shear modulus of the contact G^* using Eq. (16). Taking k_{contact} and the radius at zero applied force ($k_{\text{contact}} = 82$ N/m and $b = 1.92$ nm), we calculate $G^* = 5.3$ GPa, which, within the experimental uncertainty, is in agreement with the value of $G^* = 7.0$ GPa calculated from bulk material properties.[17,24]

To further investigate the measurement of contact radius using the tip-sample contact stiffness, we intentionally blunted the tip by imaging at a high applied normal force (115 nN) on Si in UHV. After the experiments, the tip was imaged in the STEM [as shown in Fig. 4(b)] and a new finite element model was constructed to calculate the stiffness of the modified tip. We repeated the contact stiffness measurements on the $NbSe_2$ sample and Fig. 9 shows an example of the lateral displacement of the cantilever at a (negative) applied force of −3.3 nN. The lateral displacement of the lever relative to the sample displacement has increased (compare with Fig. 6) because both k_{contact} and k_{tip} have increased. For the data of Fig. 9, we find the lateral force acting on the contact to be $F_{\text{lateral}} = 7.7$ nN and the contact stiffness $k_{\text{contact}} = 158$ N/m. Not surprisingly, the value of contact stiffness is considerably larger than the values found previously for a sharp tip.

After blunting, the force required to separate the tip from the $NbSe_2$ sample increased to $P_c = 21.9$ nN. Taking the value used previously for the interaction distance ($z_0 = 0.2$ nm) and the radius of curvature of the modified tip, as measured from STEM images ($R_{\text{tip}} = 45$ nm), we calculate Maugis-Dugdale values of $\lambda = 0.3$ and $w = 0.087$ J/m^2. The value of the elasticity parameter λ has increased due to the larger radius of curvature of the tip. The calculated value of w is close to the value found for the original tip, which further demonstrates the consistency of the model. For the data of Fig. 9 (i.e., at $P = -3.3$ nN) the effective contact radius calculated using the Maugis-Dugdale theory is $b = 3.34$ nm, from which we calculate $G^* = 5.9$ GPa, using Eq. (16), which again, within the experimental error, is in agreement with the bulk value of $G^* = 7.0$ GPa.

C. Sliding frictional force measurements

If the amplitude of the lateral sample displacement Δx is increased, then the degree of slip increases and the plot of lateral force versus displacement deviates from the linear relation observed for small lateral forces. If the lateral force acting on the contact exceeds the limiting force of friction, the tip begins to slide and the lateral force acting on the contact, tip, and cantilever becomes a constant (i.e., the limiting force of friction). These effects can be observed experimentally[25] as shown in Fig. 10, which depicts the lateral response of the cantilever (after blunting the tip) resulting from a lateral sample displacement of $\Delta x = 110$ Å peak to peak. Note that each half period of the lateral displacement signal has a similar shape to Fig. 2(b). The curved section of the lever displacement signal corresponds to the region of microslip between the tip and sample. The limiting force of friction is given by half the peak to peak amplitude

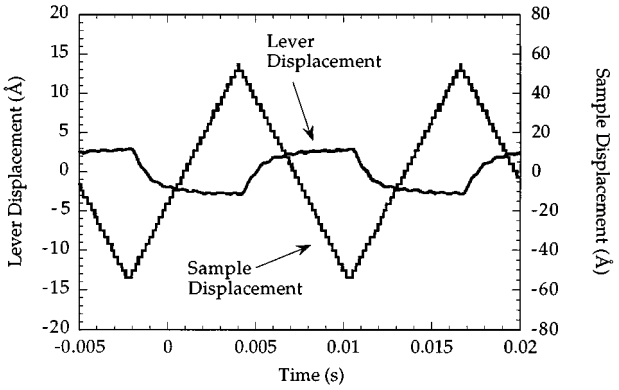

FIG. 10. Lateral response of cantilever due to the 110-Å peak to peak displacement of the $NbSe_2$ sample. The applied normal force is 35 nN.

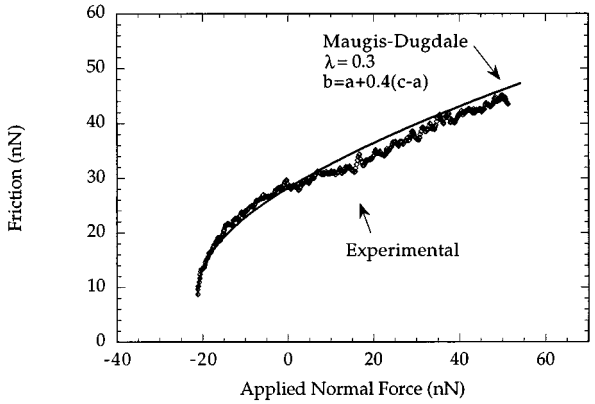

FIG. 12. Friction versus normal force with the blunt Si tip on $NbSe_2$. The sample displacement is 110 Å peak to peak. The solid line shows the Maugis-Dugdale fit to the data.

of the lateral force wave form. A lock-in amplifier can therefore be used to continually measure the peak to peak value of the input wave form. Note, however, that as the applied force changes the limiting force of friction also changes, and as such the shape of the lateral force wave form changes. This variation in the shape of the input wave form must be taken into account when calculating the friction force using the output of a lock-in amplifier. At a sufficiently high load and a fixed lateral sample displacement, the tip movement reverts from the sliding regime back to the regime of static microslip. It is therefore important to monitor the lateral displacement wave form on an oscilloscope during each experiment to ensure that the tip is always sliding.

Force distance curves can be obtained to study how the static friction varies with normal force. For the Si on $NbSe_2$ system, we have found the same relationship between friction and applied normal force during loading and unloading. Figures 11 and 12 show representative results of friction experiments before and after blunting the tip, respectively. The friction force and the adhesive force are larger for the blunder tip, as expected. More importantly, we note that the variation of friction with applied force is nonlinear and even at the smallest applied normal force P_c the friction force is appreciable. These observations arise from the single asperity nature of the contact. In contrast, in macroscopic friction experiments, one expects the friction to be proportional to the applied force. We note that the friction data is less noisy than the contact stiffness data; see Fig. 8. This occurs because the friction force is measured directly, whereas the contact stiffness is calculated from the lateral force using Eq. (17), which is very sensitive to noise when the contact stiffness is comparable to the combined lateral tip and cantilever stiffness. Experimental noise is further compounded in the contact stiffness measurements because small-amplitude displacements must be used and this results in smaller angular deflection signals than those found in the friction measurements.

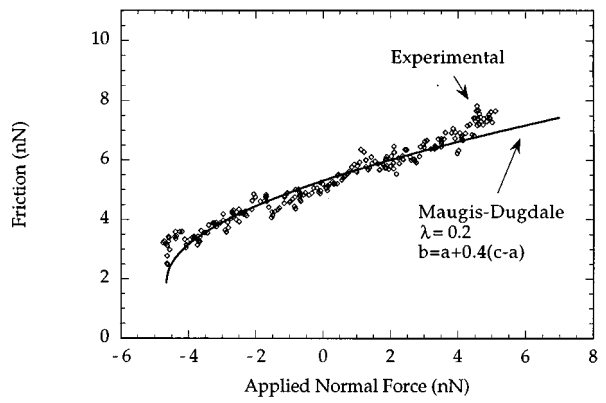

FIG. 11. Friction versus normal force with the sharp Si tip on $NbSe_2$. The sample displacement is 22 Å peak to peak. The solid line shows the Maugis-Dugdale fit to the data.

In order to compare the Maugis-Dugdale theory with the friction data, we assume that the frictional force is proportional to the tip-sample contact area, i.e., $F_{\text{friction}} = \tau A = \tau\pi b^2$. Hence we can compare the Maugis-Dugdale relationship between contact area πb^2 and normal force to the experimental friction data using the measured pull off force P_c and scaling to one data point on the friction versus normal force curve. (We use the friction data at $P = 0$.) The justification of this approach is the quality of the fit between the experimental data and the theory. We have fitted the Maugis-Dugdale theory to the friction data of Figs. 11 and 12 using the same parameters as in the contact stiffness measurements, i.e., $b = a + 0.4(c - a)$, $\lambda = 0.2$ for the original tip, and $\lambda = 0.3$ for the blunt tip. Both sets of experimental data are in good agreement with the theoretical curves. It is worth noting that for the sharp tip, the pull-off force measured from the friction data is lower than the value measured from the contact stiffness data. This is consistent with the theory that sliding results in an effective reduction in the tip-sample contact area.[7] This effect was not observed in the data taken after the tip had been blunted.

The agreement between the experimental friction data and the Maugis-Dugdale theory provides strong evidence that our central assumption $F_{\text{friction}} = \tau A$ is valid for a single asperity contact of nanometer dimensions, at least for the materials studied here. The proportionality constant τ is the shear strength of the tip-sample contact. If we take the contact area to be that given by the Maugis-Dugdale theory, we can calculate the value of the proportionality constant for our experimental data. Using the area and friction force found at

zero applied normal force, we find $\tau = 6.1 \times 10^8$ N/m^2 for the data taken with the sharp tip and $\tau = 6.6 \times 10^8$ N/m^2 after blunting the tip. We can write the theoretical shear strength of the contact as $\tau = G/\alpha$, where G is the bulk shear modulus and the parameter α is expected to have a value of about 30.[26] Using the experimental values of τ and taking the smaller bulk shear modulus of the two materials in contact ($G = 17.4$ GPa for the plane perpendicular to the c axis of $NbSe_2$), we find $\alpha = 29$ for the data taken with the sharp tip and $\alpha = 26$ for the data taken with the blunt tip. That is, the experimental shear strengths are very close to the estimated theoretical shear strength. In marked contrast, for bulk materials the theoretical shear strength is several orders of magnitude larger than the measured values.[27] The difference between the theoretical value and the value measured from bulk samples is attributed to the presence of defects, that dramatically reduce the shear strength. For example, if the defect density is drastically lowered, as in certain specially prepared single-crystal whiskers, the shear strength has been found to be much closer to the theoretical value.[27] Therefore, if we consider that the contact radii in our experiments are on the order of a few nanometers, it seems reasonable that the measured shear strength is close to the theoretical value. This is also consistent with the results of scanning tunneling microscopy experiments on nanometer-sized gold necks, in which the measured yield strength of the neck was found to be more than an order of magnitude larger than that of the bulk material.[28]

VI. CONCLUSION

To summarize, we have found good agreement between the variation in contact radius with applied force, as found experimentally by measuring the contact stiffness, and the variation predicted by the Maugis-Dugdale theory. The major difficulty with this approach to measuring the contact area, that of finding k_{tip} using a high-resolution STEM and finite element modeling, could potentially be avoided by using sharp tips with low aspect ratios. This would also increase the range of applied normal forces that could be investigated using this technique. A further difficulty is that G^* is not known. However, the comparison between theory and experimental also showed that a value of G^* calculated from the bulk material properties is reasonable.

In comparison with the contact stiffness data, the experimental signal-to-noise ratio is better in the friction measurements because of the larger amplitudes involved. Here also, we found the variation in friction with applied normal force to be in good agreement with the variation in contact area predicted by the Maugis-Dugdale theory. To relate friction and contact area we used Bowden and Tabor's assumption that friction is directly proportional to the contact area. The proportionality constant τ calculated from the experimental data was found to be in agreement with the estimated theoretical shear strength of the contact.

TABLE I. Measured values of the pull-off force P_c and calculated values of the work of adhesion w from static and sliding experiments with a silicon tip on $NbSe_2$. Two tip geometries (sharp and blunt) were used for both static and sliding experiments. The shear strength of the contact τ has been calculated from sliding data.

	Static adhesion		Sliding		
Tip radius (nm)	P_c (nN)	w (J/m^2)	P_c (nN)	w (J/m^2)	τ (N/m^2)
12	7.0	0.099	4.6	0.065	6.1×10^8
45	21.9	0.087	21.4	0.084	6.6×10^8

The experimental values of P_c, w, and τ are summarized in Table I for the two different tip shapes. The consistency of the values of w and τ and the fit to the force curves found using the two experimental methods strongly suggest that (i) the Maugis-Dugdale model provides a good basis for describing the elastic contact, which is of particular importance for AFM when the elasticity parameter $\phi \approx 1$, as the more commonly used JKR and DMT models are strictly valid only when $\phi \gg 1$ (JKR) or when $\phi \ll 1$ (DMT); (ii) for the materials studied, the assumption of Bowden and Tabor, that for dry sliding friction is proportional to contact area, is valid; and (iii) one can apply continuum mechanics down to contacts as small as 1–2 nm in radius.

Note added in proof. Similar studies are also being undertaken by R. Carpick and M. Salmeron [R. W. Carpick, D. F. Ogletree, and M. Salmeron, Appl. Phys. Lett. **70** (1997)] and we thank them for useful discussions.

ACKNOWLEDGMENTS

The authors would like to thank A. C. F. Hoole for imaging tips in the STEM and A. M. Moulin for assistance with the finite element modeling. M.L. acknowledges the support of the Sir Winston Churchill Society of Edmonton.

[1] C. M. Mate, G. M. McClelland, R. Erlandsson, and S. Chiang, Phys. Rev. Lett. **59**, 1942 (1987).
[2] F. P. Bowden and D. F. Tabor, *The Friction and Lubrication of Solids* (Clarendon, Oxford, 1950).
[3] E. Meyer, R. Luthi, L. Howald, M. Bammerlin, M. Guggisberg, and H.-J. Guntherodt, J. Vac. Sci. Technol. B **14**, 1285 (1996).
[4] R. W. Carpick, N. Agrait, D. F. Ogletree, and M. Salmeron, J. Vac. Sci. Technol. B **14**, 1289 (1996).
[5] M. A. Lantz, S. J. O'Shea, A. C. F. Hoole, and M. E. Welland, Appl. Phys. Lett. **70**, 970 (1997).
[6] D. Maugis, J. Colloid Interface Sci. **150**, 243 (1992).
[7] K. L. Johnson, Proc. R. Soc. London Ser. A **453**, 163 (1997).
[8] K. L. Johnson, *Contact Mechanics* (Cambridge University Press, Cambridge, 1985).
[9] A. R. Savkoor, *Dry Adhesive Contact of Elastomers* (Technische Universiteit Delft, Delft, 1987).
[10] M. D. Pashley, J. B. Pethica, and D. Tabor, Wear **100**, 7 (1984).
[11] K. L. Johnson, K. Kendall, and A. D. Roberts, Proc. R. Soc. London Ser. A **324**, 301 (1970).
[12] R. S. Bradley, Philos Mag. **13**, 853 (1932).

[13] V. M. Muller, B. V. Derjaguin, and Yu. P. Toporov, Colloids Surf. **7**, 251 (1983).
[14] J. B. Pethica and W. C. Oliver, Phys. Scr. **T19**, 61 (1987).
[15] Nanosensors, Wacholderweg 8, D-71134 Aldlingen, Germany.
[16] S. J. O'Shea, M. E. Welland, and T. M. H. Wong, Ultramicroscopy **52**, 55 (1993).
[17] R. Lüthi, E. Meyer, H. Haefke, L. Howald, W. Gutmannsbauer, M. Guggisberg, M. Bammerlin, H.-J. Güntherodt, Surf. Sci. **338**, 247 (1995).
[18] M. Nonnenmacher, J. Greschner, O. Wolter, and R. Kassing, J. Vac. Sci. Technol. B **9**, 1358 (1991).
[19] G. Meyer and N. M. Amer, Appl. Phys. Lett. **57**, 2089 (1990).
[20] Part No. 10-05-006 SC/4D, Graseby Optronics, 12151 Research Parkway, Orlando, FL 32826-3207.
[21] S. Grafstrom, M. Neitzert, T. Hagen, J. Ackermann, R. Neumann, O. Probst, and M. Wortge, Nanotechnology **4**, 143 (1993).
[22] T. A. Brunt, E. D. Chabala, T. Rayment, S. J. O'Shea, and M. E. Welland, J. Chem. Soc., Faraday Trans. **92**, 3807 (1996).
[23] W. C. Young, *Roark's Formulas for Stress and Strain*, 6th ed. (McGraw-Hill, New York, 1989).
[24] J. L. Feldman, Phys. Rev. B **25**, 7132 (1982).
[25] C. M. Mate, IBM J. Res. Dev. **39**, 617 (1995).
[26] A. Cottrell, *Introduction to the Modern Theory of Metals* (Institute for Metals, London, 1988).
[27] D. J. Barber and R. Loudon, *An Introduction to the Properties of Condensed Matter* (Cambridge University Press, Cambridge, 1989).
[28] A. Stalder and U. Durig, J. Vac. Sci. Technol. B **14**, 1259 (1996).